



ELSEVIER

Available online at www.sciencedirect.com

SCIENCE @ DIRECT®

Physica D 176 (2003) 19–43

PHYSICA D

www.elsevier.com/locate/physd

Geometry and boundary control of pattern formation and competition

Shuguang Guan^a, C.-H. Lai^a, G.W. Wei^{b,c,*}

^a Department of Physics, National University of Singapore, Singapore 117543, Singapore

^b Department of Computational Science, National University of Singapore, Singapore 117543, Singapore

^c Department of Mathematics, Michigan State University, East Lansing, MI 48824, USA

Received 3 October 2001; accepted 16 September 2002

Communicated by R.P. Behringer

Abstract

This paper presents the effective control of the formation and competition of cellular patterns. Simulation and theoretical analyses are carried out for pattern formation in a confined circular domain. The Cahn–Hilliard equation is solved with the zero-flux boundary condition to describe the phase separation of binary mixtures. A wavelet-based discrete singular convolution algorithm is employed to provide high-precision numerical solutions. By extensive numerical experiments, a set of cellular ordered state patterns are generated. Theoretical analysis is carried out by using the Fourier–Bessel series. Modal decomposition shows that the pattern morphology of an ordered state pattern is dominated by a principal Fourier–Bessel mode, which has the largest Fourier–Bessel decomposition amplitude. Interesting modal competition is also observed. It is found that the formation and competition of cellular patterns are effectively controlled by the confined geometry and boundary condition.

© 2002 Elsevier Science B.V. All rights reserved.

Keywords: Controlling pattern formation; Fourier–Bessel analysis; Circular domain; Cahn–Hilliard equation

1. Introduction

The synthesis and design of nanometer scale structures have attracted extensive research interest in the past few years [1]. These nanometer scale structures include a host of nanophase, multifunctional materials such as functional ceramics, functional films, supramolecular electronic packages, magnetic storage devices, and polymeric drug delivery systems. Moreover, much effort has been devoted to the design of quantum wires and quantum dots with specific properties by scientists and engineers. Physically, phase separation and pattern formation, which occur in many binary systems such as alloys, glasses and polymers, etc., play an important role in nanometer scale molecular assembly and synthesis. For example, the construction of highly ordered nanocomposites with hexagonally packed cylinder morphology has been accomplished by the phase separation of polymers [2]. It is shown

* Corresponding author. Present address: Department of Mathematics, Michigan State University, East Lansing, MI 48824, USA.

Tel.: +1-517-353-4689; fax: +1-517-432-1562.

E-mail address: wei@math.msu.edu (G.W. Wei).

that self-organization is a crucial factor in the microscopic design of smart nano-materials [3]. Modern science and technology enable the control to be carried out at the nanometer scale, or even at the molecular level which leads to various functional materials [4]. Recently, a general experimental approach for controlled self-assembly of spherical and cylindrical supermolecules has been reported [2,5]. Experiment shows that boundary-confined polymerizations can lead to thin films which possess properties dramatically different from those of the ordinary polymer [6].

Obviously, a theoretical study of the corresponding control process is an interesting subject. It is believed that the morphology of boundary-adapted polymeric self-assembly can be observed both experimentally and numerically if the characteristic length of the microphase (i.e. the characteristic length of the supra- and/or supermolecules) is comparable with the size of the confined domain. In terms of nonlinear dynamics, such a case corresponds to the “small system” regime. In this regime, usually the confining geometry plays an important role in pattern formation and selection [7]. Moreover, the phase separation process can be effectively controlled by the boundary conditions. For a binary mixture, the spatial distribution of the individual component in the boundary region may be very inhomogeneous. One component of the binary mixture might preferentially segregate to the confining surface so as to minimize the total free energy, which involves material properties of both the binary mixture and the confining surface [6]. Theoretically, this can be simulated by an appropriate boundary condition in association with a suitable mathematical model.

The control of pattern formation has attracted much attention not only for the theoretical understandings but also for the potential applications. For example, the method of directional quenching has been used to control the microphase separation of diblock copolymer [8]. Spectral techniques have been used in the control of transverse optical patterns and optical turbulence [9,10]. It was also found that the geometric size of the system can be useful in controlling the formation of optical patterns [7]. Moreover, with the rapid development of nano-technology, pattern formation now can be controlled at nanometer scale [11] or even be manipulated at the molecular level [4], resulting in new surface and bulk nanostructured materials with unique or superior properties. In a more general sense, the control and synchronization of dynamic systems, especially in the low-dimensional cases, have been extensively studied in the last decade [12]. Very recently, the control mechanism has been investigated in the continuous spatially extended systems [13–15].

The objective of the present work is to investigate the control of pattern formation and competition in a confined circular domain. The use of the circular domain is based on the following considerations. First, circular domain is a natural and important geometry for many physical systems. Extensive experiments on pattern formation have been carried out in circular domains, including surface waves [16,17], Rayleigh–Bénard convections [18,19], Taylor–Couette flow [20], combustion flames [21] and vibrated granular materials [22,23]. The rich physics exhibited in these experiments leads us to believe that controlled pattern formation in binary systems in a circular domain deserves a systematic investigation. Secondly, most of the existing theoretical studies of pattern formation in binary systems are carried out in rectangular domains. We believe that the domain geometry and boundary condition play important roles in the pattern-forming processes, such as thermal and mass diffusion, especially in the “small system” regime. It can be expected that the phase separation and pattern formation in a small domain will dramatically differ from that in a large one. In the present study, we particularly examine the effect of using both confining geometry and boundary condition as controlling factors for regulating pattern morphology and modal selection. Pattern formation through phase separation is studied by using the Cahn–Hilliard equation as a theoretical model. The importance of choosing an appropriate boundary condition is emphasized. Our long-term goal is to simulate the microscopic self-assembly of spherical and cylindrical supermolecules synthesized on a confined domain.

The organization of this paper is as follows. Section 2 is devoted to the theoretical model, stability analysis, selection of boundary condition and computational techniques. A phenomenological model, the Cahn–Hilliard equation, is chosen for the simulation of microscopic pattern formation. A discrete singular convolution (DSC) algorithm [24–27] is used in the present simulation to perform high-precision numerical integrations. The selection

of appropriate boundary conditions is discussed. The results of numerical simulations are presented in [Section 3](#). A complete set of cellular ordered state patterns have been observed by varying the control parameter, i.e., the size of the geometric domain. In [Section 4](#), the Fourier–Bessel analysis is carried out to analyze the ordered state patterns observed in the numerical experiments. This paper ends with a conclusion in [Section 5](#).

2. Theoretical and computational aspects

A model is a crucial element for theoretical analysis. In this section, we discuss a phenomenological model and its stability analysis. The use of appropriate boundary conditions is discussed and the method of solution is presented.

2.1. The model

It is well known that for a binary mixture (A + B), the dynamics of the pattern formation and phase separation is described by the Cahn–Hilliard equation (for a review, see [\[28\]](#) [\[29–31\]](#)). Its dimensionless form reads

$$\frac{\partial \Psi}{\partial t} = \frac{1}{2} \nabla^2 (-\nabla^2 \Psi - \Psi + \Psi^3), \quad (1)$$

where $\Psi(\mathbf{r}, t)$ ($|\Psi(\mathbf{r}, t)| \leq 1$) is a conserved scalar order parameter. It is usually chosen to be the difference between the local densities of components A and B.

The Cahn–Hilliard equation is a nonlinear partial differential equation. Due to the nonlinearity and the fourth-order derivative, no general analytical solution is available at the present time. Although analytical approximation approaches are very useful for understanding asymptotic behaviors, they often have limited regions of validity (for a review, see [\[28\]](#)). Accordingly, numerical simulation provides comprehensive theoretical understanding of the Cahn–Hilliard equation and the underlying physics. Throughout this paper, we will use [Eq. \(1\)](#) as a theoretical model.

So far, most simulations were carried out on rectangular domains partly for computational simplicity. Motivated by experimental results [\[5,6\]](#), we integrate the Cahn–Hilliard equation in a circular domain to simulate the microscopic phase separation and pattern formation, which is the underlying physics of the spherical and cylindrical molecular assembly. With the circular domain, it is expected that certain symmetric patterns would appear in the final ordered states. The appearance of these patterns should be greatly influenced by the size of the confined computational domain and the boundary condition of the model equation.

2.2. Linear stability analysis

Linear stability analysis is a useful tool for investigating the long wavelength instability in the process of pattern formation in spatially extended systems. It is assumed that the system is near the reference uniform steady state $\Psi(\mathbf{r}, t) = 0$ which corresponds to the homogeneously mixed state of the binary mixture. For small fluctuations of the order parameter Ψ , a separation of variables is possible and the solution has the form of

$$\Psi = \Psi_0 e^{\omega t} e^{i\mathbf{k}\cdot\mathbf{r}}. \quad (2)$$

By substituting this into the linearized Cahn–Hilliard equation, one obtains the following dispersion relation:

$$\omega(k) = -\frac{1}{2}(k^4 - k^2), \quad (3)$$

where $k = |\mathbf{k}|$. The dispersion relation is schematically shown in [Fig. 1](#). According to [Fig. 1](#), any mode with $k < k_c = 1$, will be linearly unstable because $\omega(k) \geq 0$. Activated by the small fluctuations of the order parameter,

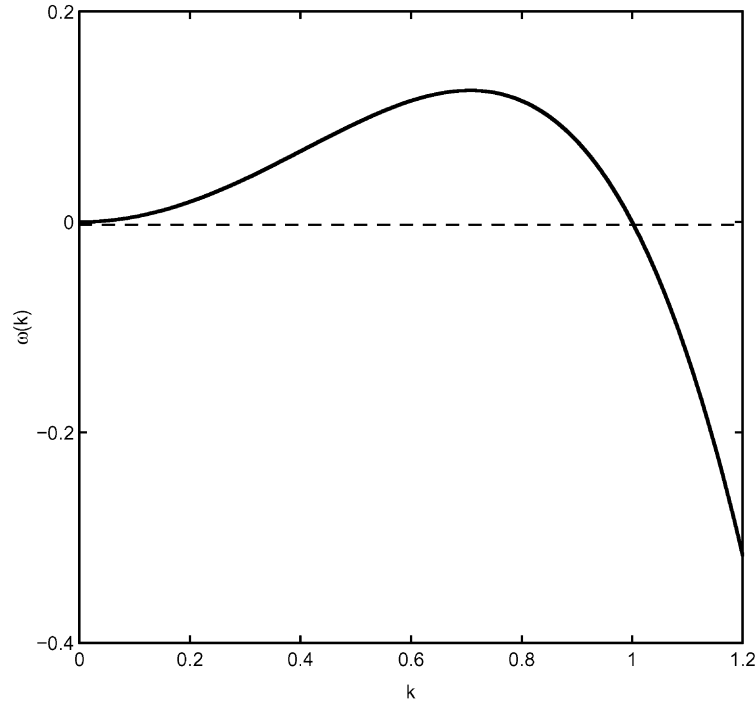


Fig. 1. Linear dispersion relation of the Cahn–Hilliard equation.

the instability arising at the microscale is able to organize the system into macroscale domains. Thus the spatially coherent states (or spatiotemporal patterns) can be established due to the balance of linear instability and nonlinear regulation. Unlike the linear case, the nonlinearity plays an important role in the pattern formation. It not only converts the linearly decaying short wavelength modes into the growing long wavelength ones, but also regulates the exponentially growing tendency of long wavelength modes. As a result, patterns of certain characteristic wavelength will be stabilized. Physically, this process corresponds to the formation of relatively large macrophase domains.

2.3. Boundary conditions

Mathematically, as a fourth-order differential equation, it takes two boundary conditions at each side of a finite domain to uniquely determine the solution of Eq. (1). The boundary conditions can be differential equations having derivatives of the order from 0 to 3. In fact, the spatial behavior of the Cahn–Hilliard equation is mainly influenced by the biharmonic equation $\nabla^4 w(x, y) = \omega^2 w(x, y)$, which is the governing equation for the Kirchhoff plate [32]. In vibration analysis, four types of standard boundary conditions are often used for the biharmonic equation in rectangular domain [32], i.e.:

- simply supported edge:

$$w = 0, \quad \frac{\partial^2 w}{\partial n^2} + \nu \frac{\partial^2 w}{\partial s^2} = 0, \quad (4)$$

- clamped edge:

$$w = 0, \quad \frac{\partial w}{\partial n} = 0, \quad (5)$$

- free edge:

$$\frac{\partial^2 w}{\partial n^2} + \nu \frac{\partial^2 w}{\partial s^2} = 0, \quad \frac{\partial^3 w}{\partial n^3} + (2 - \nu) \frac{\partial^3 w}{\partial n \partial s^2} = 0, \quad (6)$$

- and transversely supported edge with nonuniform elastic rotational restraint:

$$w = 0, \quad -D \left(\frac{\partial^2 w}{\partial n^2} + \nu \frac{\partial^2 w}{\partial s^2} \right) = K(s) \frac{\partial w}{\partial n}, \quad (7)$$

where ν is Poisson's ratio, $K(s)$ the varying elastic rotational stiffness of the plate elastic edge and n and s denote, respectively, the normal and tangential coordinates with respect to the plate edge. These studies not only give us an indication of the possible complexity of the boundary conditions for the present simulation but also offer a physical interpretation for potential boundary conditions.

The problem of solving the Cahn–Hilliard equation with appropriate boundary conditions has, to our knowledge, rarely been discussed in the literature. The boundary conditions used in structural analysis cannot be directly employed in the present study, although they provide a guidance for our selection. Of primary importance to the present study is the conservation of the order parameter, i.e., the order parameter should obey the following constraint at any time:

$$\int_{\Omega} d\mathbf{r} \Psi(\mathbf{r}, t) = C, \quad (8)$$

where Ω is the domain of interest and C is a constant. In the present study, we consider only equal ratio composition, i.e., $C = 0$ in Eq. (8). This implies that the possible morphology in this system is the polarization of the order parameter.

Another important physical constraint on the order parameter is

$$\sup |\Psi(\mathbf{r}, t)| \leq 1 \quad \forall \mathbf{r} \in \Omega, \quad t \in [0, \infty]. \quad (9)$$

However, as a generalized reaction–diffusion equation, the Cahn–Hilliard equation does not automatically satisfy Eq. (9). All unphysical solutions are to be excluded from the present integration numerically.

It remains to choose two other conditions to determine the solution uniquely. To this end, many conditions used in the plate analysis are possible candidates. In particular, both the Dirichlet and Neumann boundary conditions have simple physical interpretations for the present phase separation. For example, the Dirichlet boundary condition

$$\Psi(\mathbf{r}_b, t) = 0 \quad (10)$$

implies that there is no phase polarization at the boundary. (Here \mathbf{r}_b denotes the domain boundary.) The pattern formation of the Cahn–Hilliard equation under conditions (8)–(10) was studied in the literature. In the present paper, we consider an alternative choice.

It is well known that the Cahn–Hilliard equation is akin to the time-dependent Ginzburg–Landau equation. In particular, the Cahn–Hilliard equation can be viewed as a special case derived from the minimization of the Ginzburg–Landau type free energy F

$$F(\Psi) = \int_{\Omega} [f(\Psi) + K(\nabla\Psi)^2] d\mathbf{r}, \quad (11)$$

where Ω is the domain of interest, K a positive parameter and $f(\Psi)$ the free energy per unit volume. Noveick-Cohen and Segel [31] argued that the zero-flux boundary condition

$$\frac{\partial \Psi}{\partial n} = 0, \quad (12)$$

is a prerequisite for arriving at Eq. (11). Here, the direction of the coordinates n is normal to the boundary surface. Therefore, a complete set of boundary conditions can be given by Eqs. (8), (9) and (12). Physically, boundary selection and boundary segregation [6] can be simulated by the zero-flux boundary condition.

2.4. Numerical aspects

Integrating the Cahn–Hilliard equation in a circular computational domain is not an easy task. It is necessary to integrate the governing equation in polar coordinates (r, θ) , so that the $O(2)$ symmetry is preserved. Due to the lack of periodic boundary conditions, Fourier spectral methods cannot be directly applied. In polar coordinates, the derivative

$$\nabla^4 = \partial_{rrrr} + 2r^{-1}\partial_{rrr} - r^{-2}\partial_{rr} + r^{-3}\partial_r + 2r^{-2}\partial_{rr\theta\theta} - 2r^{-3}\partial_{r\theta\theta} + 4r^{-4}\partial_{\theta\theta} + r^{-4}\partial_{\theta\theta\theta\theta} \quad (13)$$

causes artificial singularities up to fourth order at the origin. Conventional local methods, such as finite elements and finite differences encounter difficulties of insufficient accuracy. Moreover, the nonlinear terms may cause additional complexity in the phase space geometry. Therefore, it is technically very demanding to integrate the Cahn–Hilliard equation in the circular domain. In the present simulation, we overcome these numerical difficulties by utilizing a wavelet-based DSC algorithm [24–27]. The DSC algorithm has been successfully applied in many scientific and engineering computations. For example, it has been successfully used in the integration of the sine-Gordon equation when the initial values are chosen to be close to the most excitable homoclinic orbit [26]. In the analysis of high frequency vibrations of aerospace structures, the DSC algorithm is the only available approach at present that is capable of predicting tens of thousand vibration eigenmodes [27].

Due to the fourth-order derivative in space, it is efficient to employ an implicit scheme for the time integration. The standard implicit Crank–Nicolson scheme is chosen for the time discretization. The nonlinear terms are linearized by using the Newton-like technique. Coupled collocation equations are solved at each time step by a standard direct method. For all simulations, we choose 32 and 64 grid points in the r and θ directions, respectively. The DSC regularization parameters [24] are set as $\sigma_q/\Delta_q = 3.8$ ($q = r, \theta$) in both directions. The DSC bandwidth parameters are set to 30 in both dimensions. The initial order parameter field Ψ_0 is given by random noise of small amplitudes (about 10^{-2}) inside the computational domain. In this simulation, the boundary conditions described in the last subsection, i.e., Eqs. (8), (9) and (12), are implemented. Since the Cahn–Hilliard equation has no intrinsic control parameters, we use the geometric control parameter, i.e., the radius R of the circular domain, to regulate the pattern morphology. Due to the numerical limitation in computer memory and time, our simulations focus on the small and moderately large geometric sizes. (Any increase in the domain size requires enlarging the computational grids.) The control parameter ranges from 1 to 13. At each given radius, Eq. (1) was integrated up to 1000 time steps, and some particular runs were integrated up to 2000 time steps. In order to maintain a spectral level of accuracy, the computations are extremely expensive and time consuming in terms of computer resources.

3. Pattern morphology

Fig. 2 shows the mesh and contour plots of the ordered state patterns. These cellular patterns are obtained by long time propagations of the initial random state with different control parameters R . Initially, we systematically explore the R values from 1 to 13 with a typical step size of 0.5. Then a few more runs with a smaller step size (about 0.1) are added to locate some “expected” ordered state patterns at certain radii. By extensive numerical

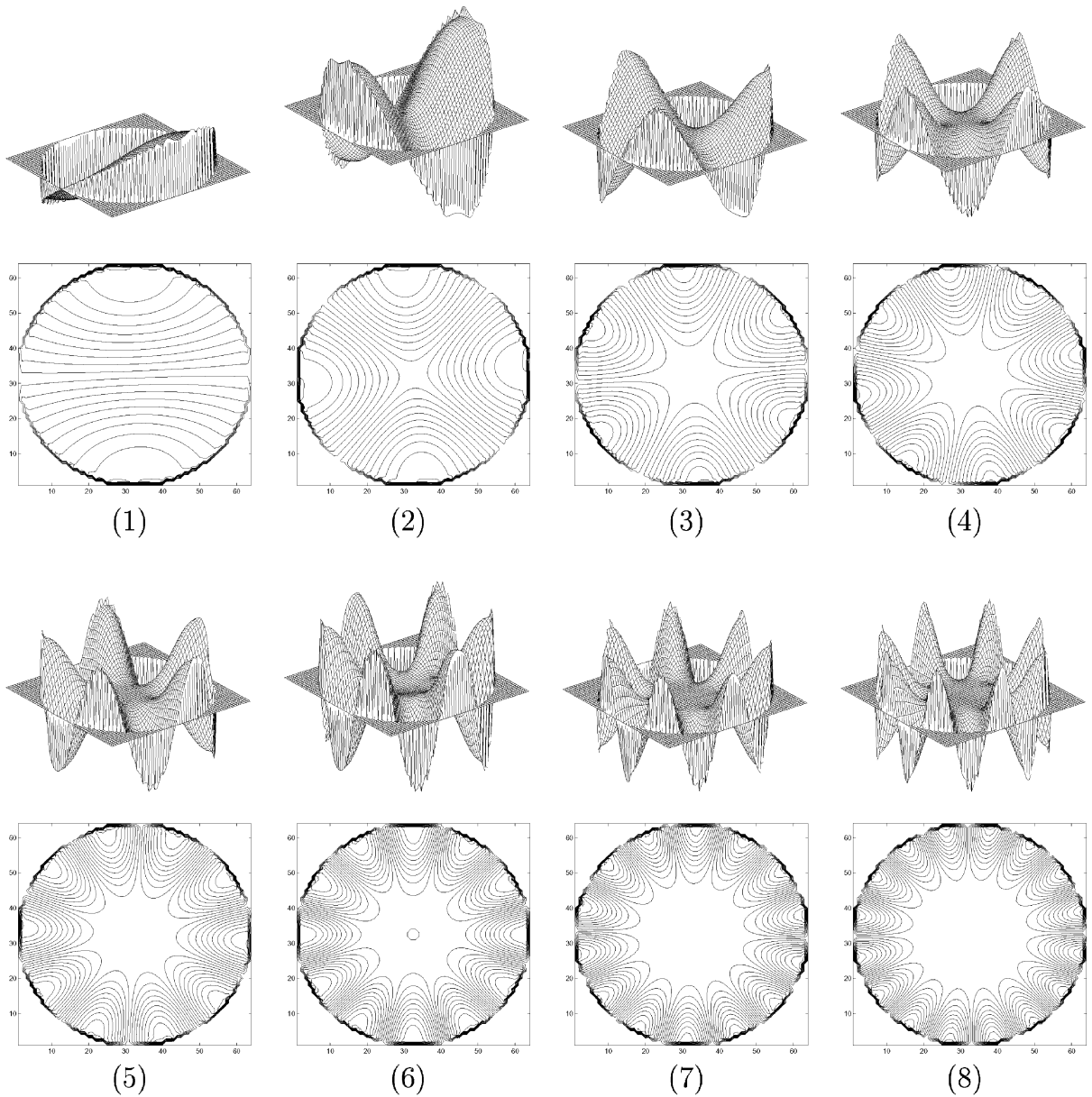


Fig. 2. Mesh and contour plots of the typical ordered state patterns and the initial values: (1) [1, 1] ($t = 500$); (2) [1, 2] ($t = 1000$); (3) [1, 3] ($t = 1000$); (4) [1, 4] ($t = 700$); (5) [1, 5] ($t = 1170$); (6) [1, 6] ($t = 1240$); (7) [1, 7] ($t = 400$); (8) [1, 8] ($t = 440$); (9) [1, 9] ($t = 1230$); (10) [1, 10] ($t = 540$); (11) [1, 11] ($t = 1000$); (12) [1, 12] ($t = 750$); (13) [2, 0] ($t = 600$); (14) [2, 1] ($t = 1150$); (15) [2, 2] ($t = 1240$); (16) [2, 3] ($t = 1190$); (17) [2, 4] ($t = 800$); (18) [2, 5] ($t = 1250$); (19) [2, 6] ($t = 820$); (20) [2, 7] ($t = 660$); (21) [3, 0] ($t = 700$); (22) [3, 1] ($t = 920$); (23) [3, 2] ($t = 480$); (24) [3, 3] ($t = 790$); (25) [3, 4] ($t = 1220$); (26) [3, 5] ($t = 560$); (27) [4, 0] ($t = 950$); (28) [4, 1] ($t = 630$); (29) [4, 2] ($t = 990$); (30) the initial values. The corresponding control parameters are listed in Table 2.

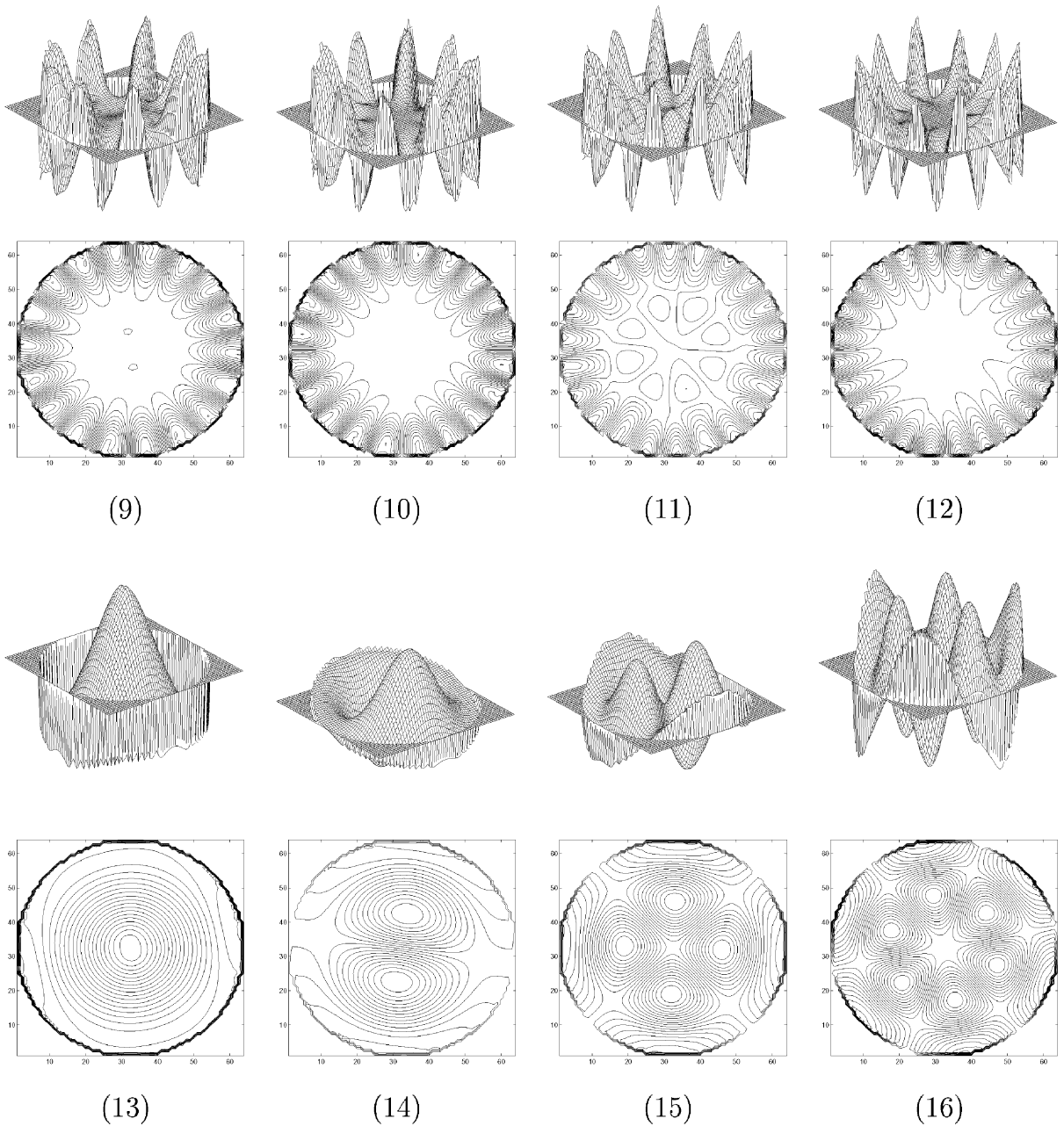


Fig. 2. (Continued).

experiments, four complete classes of ordered state patterns have been observed. It is found that all the ordered state patterns consist of several concentric rings of cells. Notably, the outermost concentric ring of the ordered state patterns actually comprises “half cells”, which is obviously seen from the contour plots shown in Fig. 2. The zero-flux boundary condition is very similar to the free edge boundary in the structural analysis. Unlike the Dirichlet

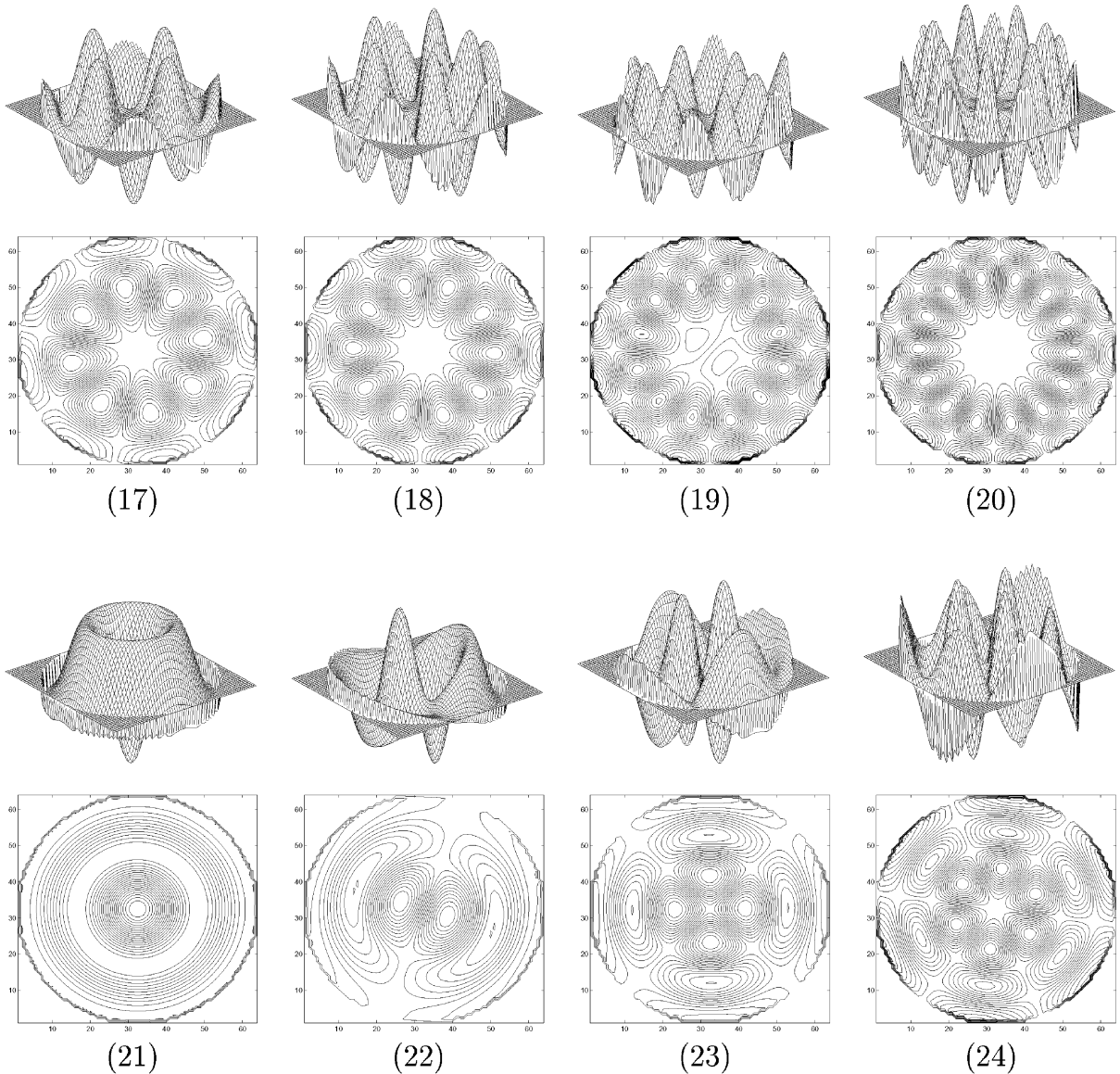


Fig. 2. (Continued).

boundary condition, it does not require specific boundary values. Eq. (12) usually leads the order parameter to attain a local extremum at the boundary. In the next section, we will offer a reasonable explanation from the point of view of the Fourier–Bessel analysis. In general, the spatial distribution of the cells is interlaced, which implies that any two neighboring cells are at different phases. Such a phase separation can be regarded as local polarization of the order parameter and it is consistent with the conservation of the order parameter, i.e., Eq. (8). Moreover, the complexity of patterns increases as the control parameter R increases, and a careful examination reveals that the ordered state patterns can be regularly classified by a pair of integers $[l, m]$ ($l = 1-4$), as shown in Fig. 2. Here l denotes the number of the concentric rings in the ordered state patterns, while m denotes the number of the

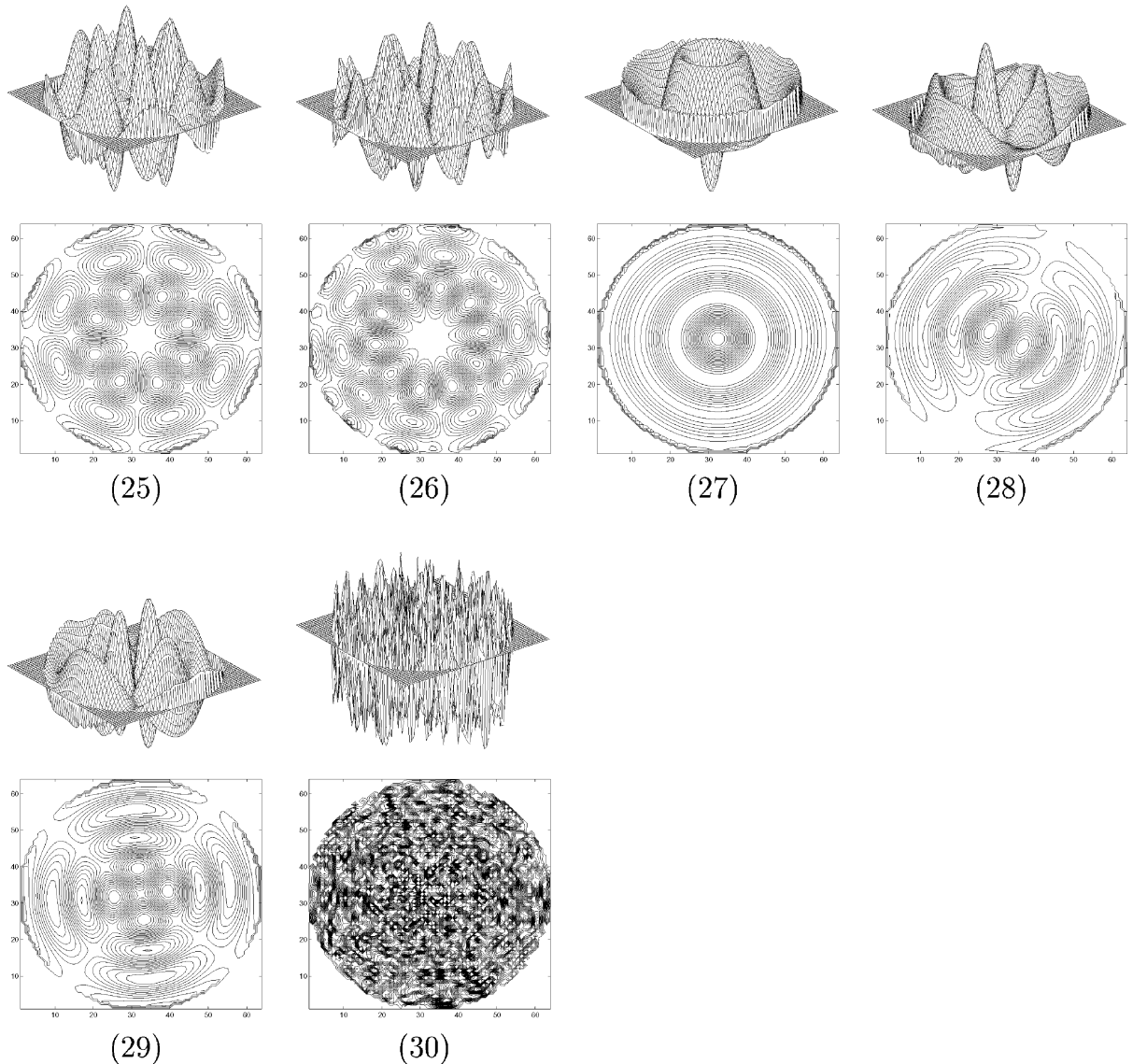


Fig. 2. (Continued).

one-phase domains in each ring. In the next section, we will show that this pair of integers $[l, m]$ is related to the Fourier–Bessel modes in the circular domain. In Fig. 2, all the four classes of ordered state patterns observed when $R \leq 13$ are plotted according to their characteristic integer pairs. The pattern $[1, 0]$ is absent in $l = 1$ series because it does not satisfy the conservation of the order parameter. In Table 2, we list all the control parameter values at which these ordered state patterns were attained. Experimentally, cellular patterns have been observed in other systems, such as convective fluids [16], combustion flames [21], and nonlinear optical media [7]. Nevertheless, due to the constraint of experimental conditions, only limited cellular pattern morphology was observed [7,16,21].

4. Fourier–Bessel analysis

In order to further investigate the pattern morphology of the ordered patterns, a quantitative analysis is needed. The linearized stationary Cahn–Hilliard equation

$$\nabla^2(\nabla^2 + 1)\tilde{\Psi} = 0 \quad (14)$$

can be factorized into the Laplace and Helmholtz equations. In polar coordinates, by the separation of variables, these two equations both lead to the Bessel equation in the r direction. Hence, a general solution to Eq. (14) can be expressed as

$$\tilde{\Psi}(r, \theta) = \sum_{m=0}^{\infty} [A_m J_m(r) + B_m N_m(r)] e^{im\theta}, \quad m = 0, 1, \dots, \quad (15)$$

where $J_m(r)$ and $N_m(r)$ are the Bessel functions of the first and the second kinds, respectively. Since the circular domain includes the origin, in order to avoid singularity at the origin, B_m must be set to zero. Thus the solution to

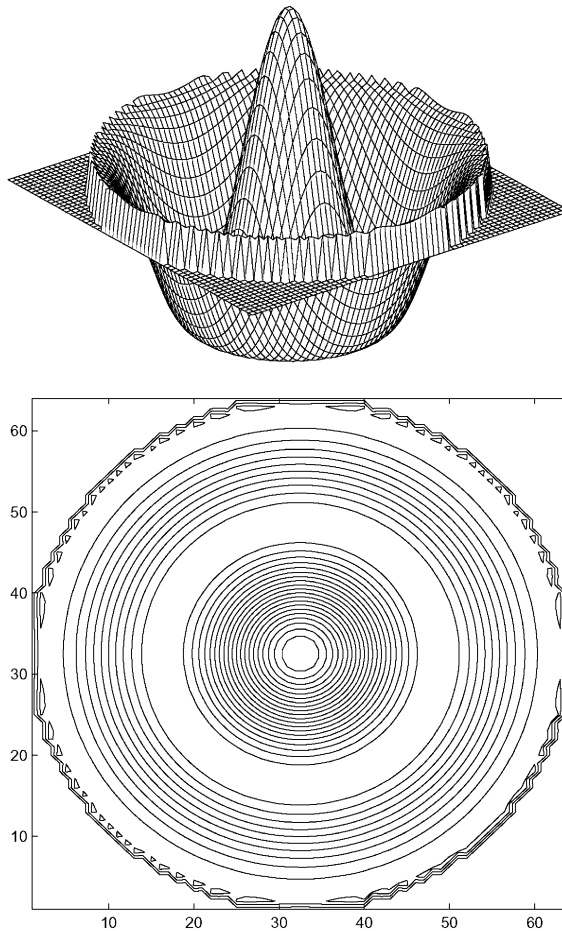


Fig. 3. Mesh and contour plots of the ordered state pattern at $R = 7.0$, $t = 550$. Its corresponding principal Fourier–Bessel mode is $[3, 0]$.

Eq. (14) is

$$\tilde{\Psi}(r, \theta) = \sum_{m=0}^{\infty} A_m J_m(r) e^{im\theta}, \quad m = 0, 1, \dots, \quad (16)$$

i.e., the linearized stationary Cahn–Hilliard equation has the solution of the Bessel functions of the first kind.

On the other hand, a careful examination of the typical ordered state patterns in Fig. 2 reveals that they resemble the Fourier–Bessel modes truncated to a certain radius in the finite circular domain. The above consideration suggests that the solution of the full Cahn–Hilliard equation with the zero-flux boundary condition in the circular domain can be expressed as a Fourier–Bessel series

$$\Psi(r, \theta) = \sum_{l,m} Z_{l,m} \Phi_{l,m}(r, \theta) + \text{c.c.}, \quad (17)$$

where

$$\Phi_{l,m}(r, \theta) = J_m\left(\frac{\mu_{l,m}r}{R}\right) e^{im\theta}, \quad m \geq 0, \quad l > 0 \quad (18)$$

is a Fourier–Bessel mode characterized by $[l, m]$, and c.c. denotes the complex conjugate. Here, $J_m(\mu_{l,m}r/R)$ is the m th Bessel function of the first kind [34] and $\mu_{l,m}$ its l th nontrivial extremum, i.e., $\{\mu_{l,m}\}$ ($l = 1, 2, \dots$) are the nontrivial roots of the equation

$$J'_m(\mu R) = 0. \quad (19)$$

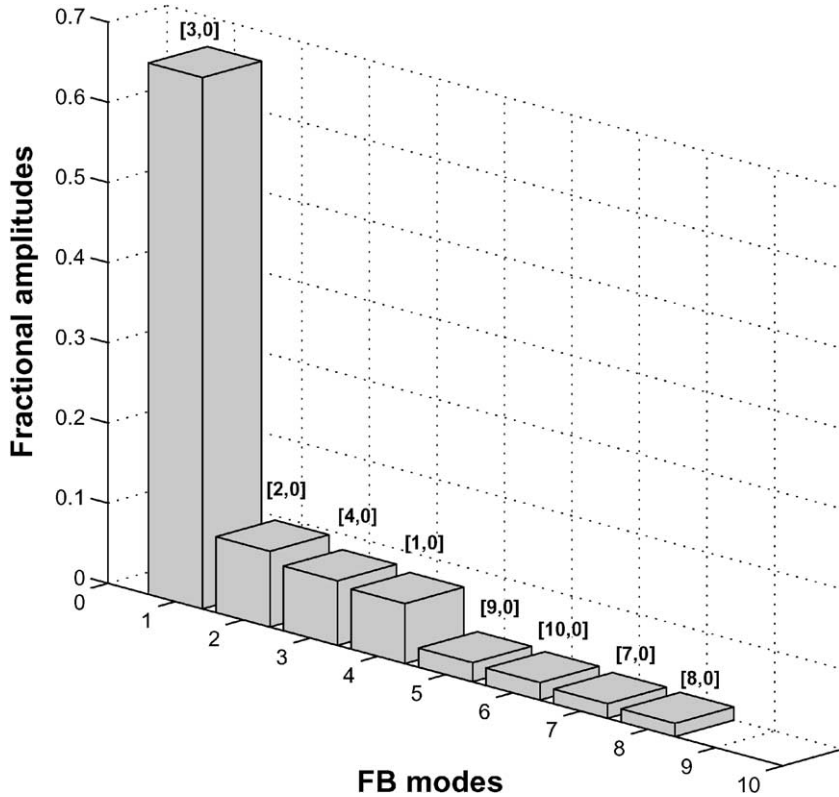


Fig. 4. Fourier–Bessel decomposition of the ordered state pattern shown in Fig. 3.

Table 1

The fractional amplitudes corresponding to the three most important Fourier–Bessel modes, as well as the entropies of the ordered state patterns shown in Fig. 2

Pattern	First	Second	Third	Pattern entropy
1	$A_{1,1} = 0.957$	$A_{10,1} = 0.00512$	$A_{1,3} = 0.00491$	0.0471
2	$A_{1,2} = 0.603$	$A_{10,2} = 0.0587$	$A_{9,2} = 0.0556$	0.271
3	$A_{1,3} = 0.805$	$A_{1,9} = 0.0435$	$A_{10,3} = 0.0624$	0.177
4	$A_{1,4} = 0.680$	$A_{10,4} = 0.0451$	$A_{9,4} = 0.0430$	0.244
5	$A_{1,5} = 0.662$	$A_{10,5} = 0.0512$	$A_{9,5} = 0.0490$	0.240
6	$A_{1,6} = 0.656$	$A_{10,6} = 0.0483$	$A_{9,6} = 0.0463$	0.252
7	$A_{1,7} = 0.878$	$A_{10,7} = 0.0525$	$A_{9,7} = 0.00883$	0.127
8	$A_{1,8} = 0.878$	$A_{2,8} = 0.0525$	$A_{10,8} = 0.00884$	0.108
9	$A_{1,9} = 0.715$	$A_{10,9} = 0.0451$	$A_{9,9} = 0.0437$	0.210
10	$A_{1,10} = 0.981$	$A_{1,14} = 0.00276$	$A_{2,6} = 0.00221$	0.0262
11	$A_{1,11} = 0.591$	$A_{3,4} = 0.0633$	$A_{1,12} = 0.0365$	0.380
12	$A_{1,12} = 0.773$	$A_{2,8} = 0.0992$	$A_{1,8} = 0.0492$	0.175
13	$A_{2,0} = 0.408$	$A_{1,0} = 0.124$	$A_{10,0} = 0.0560$	0.395
14	$A_{2,1} = 0.898$	$A_{3,1} = 0.0237$	$A_{1,1} = 0.0106$	0.102
15	$A_{2,2} = 0.611$	$A_{1,2} = 0.110$	$A_{10,2} = 0.0448$	0.260
16	$A_{2,3} = 0.650$	$A_{1,3} = 0.171$	$A_{10,3} = 0.0281$	0.224
17	$A_{2,4} = 0.763$	$A_{3,4} = 0.0660$	$A_{1,4} = 0.0241$	0.189
18	$A_{2,5} = 0.710$	$A_{3,5} = 0.0608$	$A_{10,5} = 0.0356$	0.225
19	$A_{2,6} = 0.671$	$A_{1,6} = 0.165$	$A_{4,1} = 0.0813$	0.218
20	$A_{2,7} = 0.725$	$A_{1,7} = 0.0597$	$A_{3,7} = 0.0427$	0.202
21	$A_{3,0} = 0.662$	$A_{2,0} = 0.0945$	$A_{4,0} = 0.0806$	0.217
22	$A_{3,1} = 0.717$	$A_{4,1} = 0.0990$	$A_{1,1} = 0.0447$	0.208
23	$A_{3,2} = 0.674$	$A_{4,2} = 0.0827$	$A_{2,2} = 0.0571$	0.246
24	$A_{3,3} = 0.652$	$A_{2,3} = 0.116$	$A_{1,3} = 0.102$	0.228
25	$A_{3,4} = 0.915$	$A_{4,4} = 0.0207$	$A_{1,4} = 0.0110$	0.0876
26	$A_{3,5} = 0.590$	$A_{2,8} = 0.0592$	$A_{4,5} = 0.0567$	0.381
27	$A_{4,0} = 0.667$	$A_{5,0} = 0.0857$	$A_{1,0} = 0.0586$	0.236
28	$A_{4,1} = 0.668$	$A_{5,1} = 0.0821$	$A_{3,1} = 0.0533$	0.250
29	$A_{4,2} = 0.693$	$A_{3,2} = 0.0782$	$A_{5,2} = 0.0752$	0.233

Table 2

A comparison of control parameters R used for observing the ordered state patterns and the corresponding nontrivial extrema of the Bessel functions under the zero-flux boundary condition

m	$l = 1$		$l = 2$		$l = 3$		$l = 4$	
	R	$\mu_{1,m}$	R	$\mu_{2,m}$	R	$\mu_{3,m}$	R	$\mu_{4,m}$
0	–	0	4.0	3.832	7.0	7.016	9.75	10.173
1	2.5	1.841	5.25	5.331	8.25	8.536	11.1	11.706
2	3.75	3.054	6.75	6.706	9.75	9.969	12.75	13.170
3	4.25	4.403	7.75	8.015	10.75	11.346	–	–
4	5.875	5.318	8.75	9.282	11.8	12.682	–	–
5	6.25	6.416	10.0	10.564	13.0	13.998	–	–
6	7.25	7.501	11.1	11.804	–	–	–	–
7	8.5	8.578	12.2	13.032	–	–	–	–
8	9.25	9.647	–	–	–	–	–	–
9	10.25	10.711	–	–	–	–	–	–
10	11.25	11.771	–	–	–	–	–	–
11	11.9	12.826	–	–	–	–	–	–
12	13.0	13.879	–	–	–	–	–	–

In other words, the Bessel function takes the extreme values at $\{\mu_{l,m}\}$. Under the zero-flux boundary condition, the orthonormality and completeness of the functions $\Phi_{l,m}(r, \theta)$ provide

$$Z_{l,m} = \frac{1}{\pi R^2 [1 - (m/\mu_{l,m})^2] J_m^2(\mu_{l,m})} \int_0^{2\pi} \int_0^R \Psi(r, \theta) \bar{\Phi}_{l,m}(r, \theta) r \, d\theta \, dr, \quad m > 0, \quad (20)$$

where the coefficients $Z_{l,0}$ take half of the value given by the above formula. Here the bar denotes the complex conjugate. Eq. (17) paves the way for a quantitative analysis of the ordered state patterns described in the last section. Based on Eq. (17), the Fourier–Bessel decomposition of the ordered state patterns can be carried out. In a more general perspective, Fourier–Bessel analysis [33] is suitable for the quantitative characterization of cellular patterns.

4.1. Modal control

Due to the nonlinearity of the Cahn–Hilliard equation, it is unlikely that pure Fourier–Bessel modes will occur as the solution of our theoretical model. Thus a quantitative analysis in terms of Fourier–Bessel modes is needed for the detailed composition of the ordered state patterns. This can be achieved by computing the Fourier–Bessel decomposition (expansion) coefficients $Z_{l,m}$ for each ordered state pattern. Based on the Fourier–Bessel decomposition, two quantities can be defined to characterize the ordered state patterns. The first quantity is the fractional amplitude $A_{l,m}$ captured by a Fourier–Bessel mode $[l, m]$. It is defined as

$$A_{l,m} = \frac{|Z_{l,m}|}{A}, \quad (21)$$

where $|Z_{l,m}|$ is the Fourier–Bessel decomposition amplitude of mode $[l, m]$. Here, A is the total Fourier–Bessel decomposition amplitude which denotes the sum of all Fourier–Bessel decomposition amplitudes

$$A = \sum_{l,m} |Z_{l,m}|, \quad m, l \in \mathbb{Z}, \quad m \geq 0, \quad l > 0. \quad (22)$$

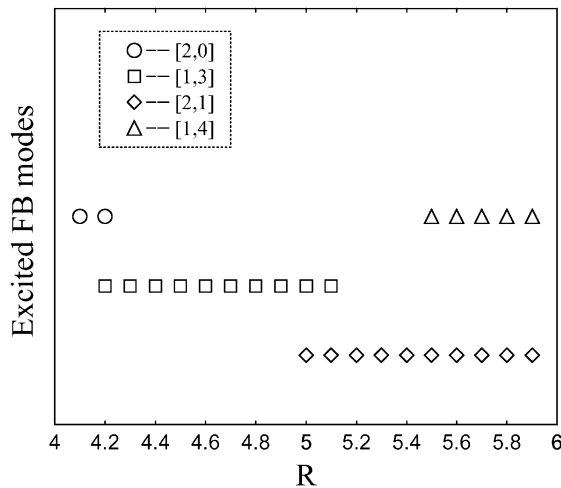


Fig. 5. Phase diagram around $R = 5.0$.

Obviously, the fractional amplitude can be understood as the “energy” captured by each Fourier–Bessel mode. The sum of fractional amplitudes approaches 1 as the number of Fourier–Bessel modes in the decomposition increases to infinity. The second quantity that can be used for characterizing the ordered state patterns is the pattern entropy

$$\epsilon = - \lim_{N \rightarrow \infty} \frac{1}{\ln N} \sum_{l,m} A_{l,m} \ln A_{l,m}, \quad (23)$$

where l, m are the indices of Fourier–Bessel modes $[l, m]$ and N the total number of Fourier–Bessel modes used in the decomposition. The pattern entropy measures the fractional amplitude distribution among the Fourier–Bessel modes and varies between 0 and 1, as the number of Fourier–Bessel modes increases. For a given ordered state pattern, the pattern entropy is relatively small when the total Fourier–Bessel decomposition amplitude, i.e., the

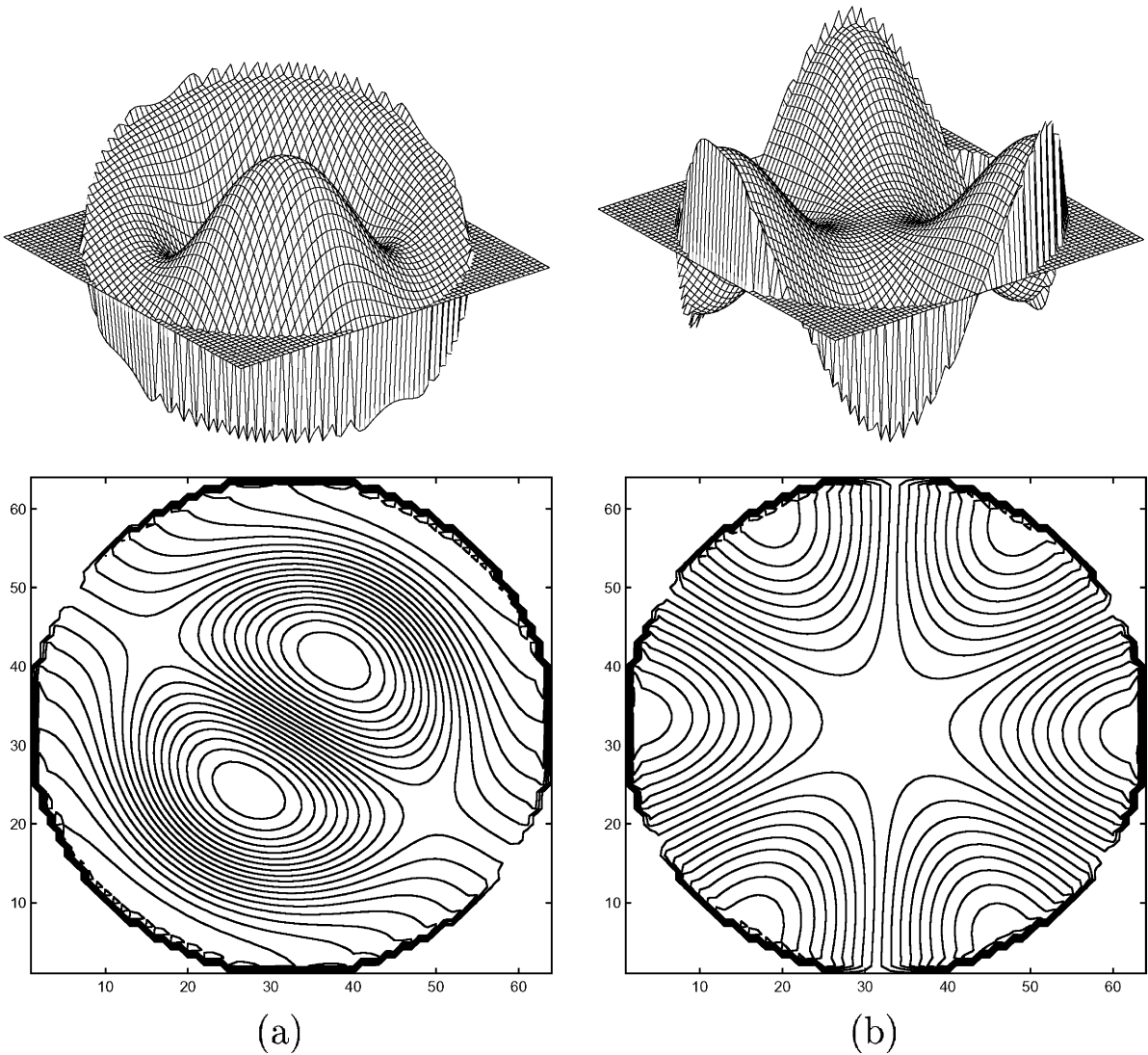


Fig. 6. Mesh and contour plots of the ordered state patterns at $R = 5.0$: (a) $[2, 1]$ ($t = 730$); (b) $[1, 3]$ ($t = 900$).

total energy of the pattern, is mainly captured by a few Fourier–Bessel modes. An extreme case is that there is only one Fourier–Bessel mode which contributes to the ordered state pattern. As such, the value of the pattern entropy will be zero according to Eq. (23). On the contrary, when the total Fourier–Bessel decomposition amplitude spreads across a large number of Fourier–Bessel modes, the value of the pattern entropy will approach 1.

Fig. 3 depicts a typical ordered state pattern. Its Fourier–Bessel decomposition is illustrated in Fig. 4, where the fractional amplitudes $A_{l,m}$ are sorted in the decreasing order and only the Fourier–Bessel modes whose fractional amplitudes are greater than 0.01 are shown. From Fig. 4, it is found that fractional amplitudes of most modes are very small (below 10^{-2}) except for a few active ones. Among eight Fourier–Bessel modes shown in the figure, there is a dominant mode whose fractional amplitude is significantly larger than those of the others.

In Table 1, the three largest fractional amplitudes and the pattern entropies are listed for all the ordered state patterns shown in Fig. 2. It is found that all the entropies are less than 0.4 and the averaged value is about 0.2. This implies that there are only a few dominant Fourier–Bessel modes contributing to the ordered state patterns. On an average, the first largest fractional amplitude is about 0.74, while the second largest amplitude is usually below 0.1. We describe this dominant Fourier–Bessel mode as *the principal Fourier–Bessel mode*, which contributes the most to the morphology of an ordered state pattern. In Fig. 2, we have classified the typical ordered state patterns according to their “quantum number”, $[l, m]$, of the principal Fourier–Bessel modes. Moreover, from Fig. 2 and Table 1, it is found that the morphology of the ordered state pattern is mainly determined by the principal Fourier–Bessel

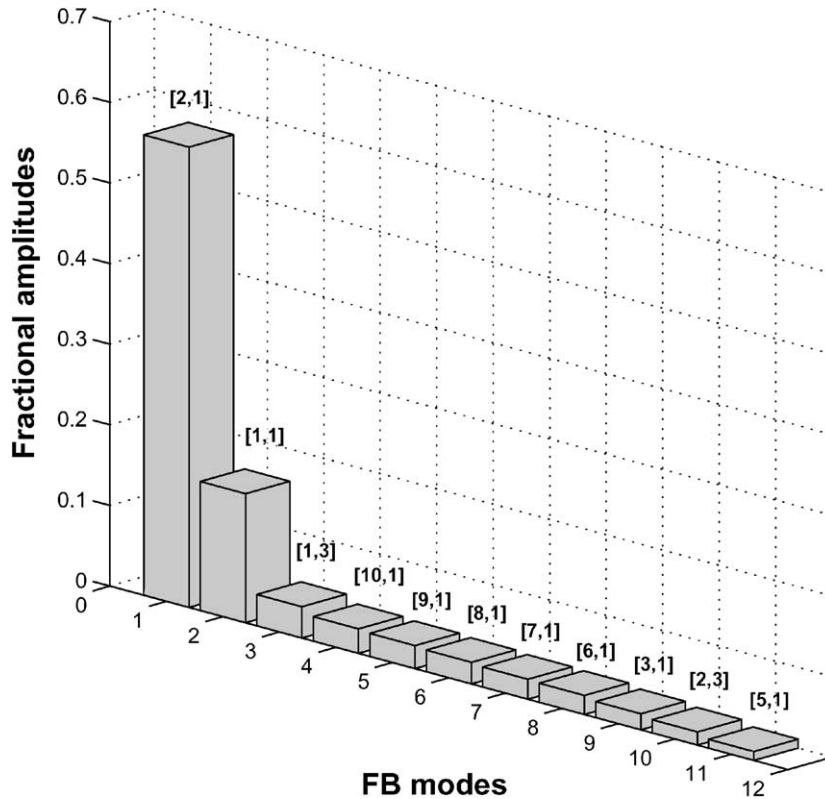


Fig. 7. Fourier–Bessel decomposition of the ordered state pattern shown in Fig. 6(a).

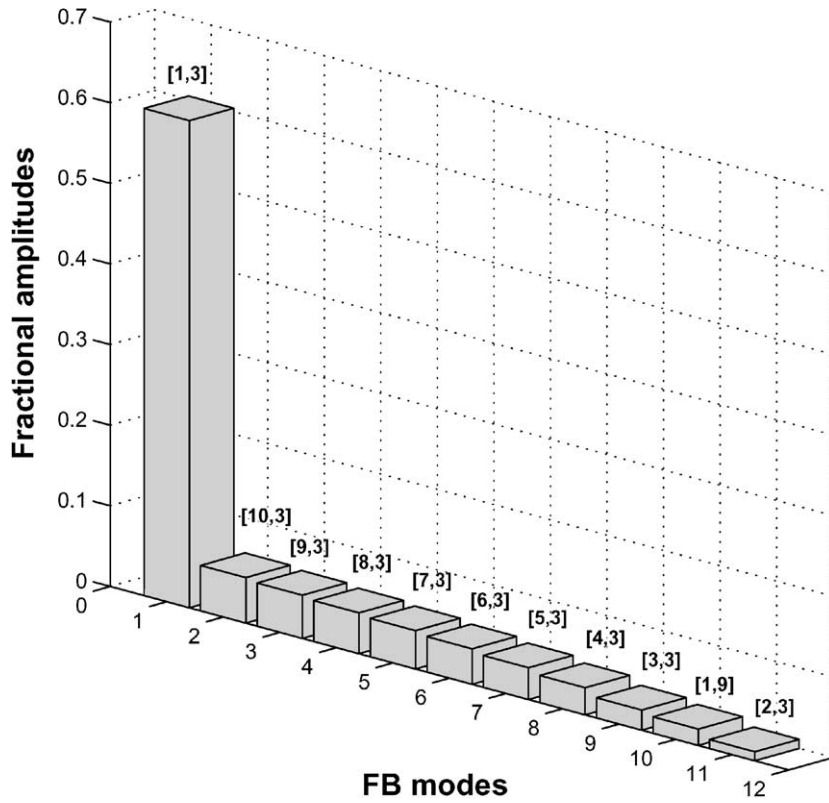


Fig. 8. Fourier–Bessel decomposition of the ordered state pattern shown in Fig. 6(b).

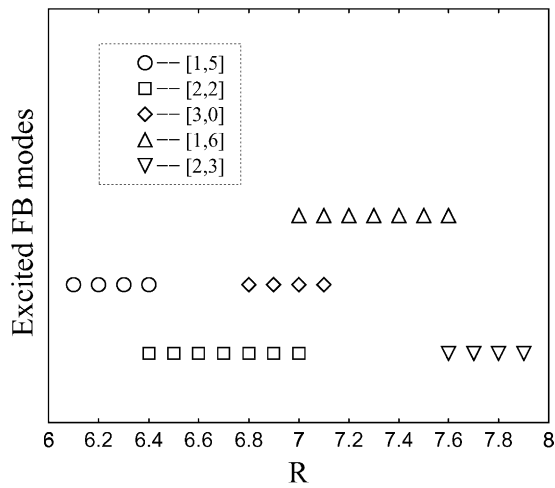


Fig. 9. Phase diagram around $R = 7.0$.

mode, whereas the contributions from the nonprincipal Fourier–Bessel modes can slightly modulate the cell shapes.

4.2. Controlled pattern selection and competition

The single phase state at $R = 0$ does not satisfy the physical constraint. According to linear stability analysis, simultaneous symmetry polarization can be induced from the initial homogeneous distribution by the random noise of an extremely small amplitude ($\sim 10^{-2}$) for an appropriate $R > 0$. Fourier–Bessel decomposition shows that an ordered state pattern is usually dominated by the principal Fourier–Bessel mode. By extensive simulations, it is found that the system tends to stabilize at a Fourier–Bessel mode $[l, m]$ when the control parameter R is close to the nontrivial extremum $\mu_{l,m}$ of the Bessel function, i.e., when R is close to the values at which the Bessel function takes the nontrivial extreme values.

The first extreme point of J_0 is at $\mu_{1,0} = 0$. However, it is a trivial point and is unphysical in the present system. The ordered state pattern $[1, 1]$ is first observed at $R = 2.5$, which is close to the theoretical extremum $\mu_{1,1} = 1.841$. For all the ordered state patterns, a comparison of R values ($R \leq 13$) at which the patterns are observed and the corresponding theoretical extreme points $\mu_{l,m}$ of the Bessel function are listed in Table 2. Although the observed R values differ slightly from the theoretical values, generally the numerical results match theoretical predictions well. Actually, in our numerical experiments we have made use of this modal selection mechanism to guide us to locate or control some “expected” patterns. Moreover, a careful examination reveals that the order of the appearance of the ordered state patterns are consistent with the interlacing of Bessel function’s extrema [34]:

$$0 < \mu_{1,m} < \mu_{1,m+1} < \mu_{2,m} < \mu_{2,m+1} < \mu_{3,m} < \dots$$

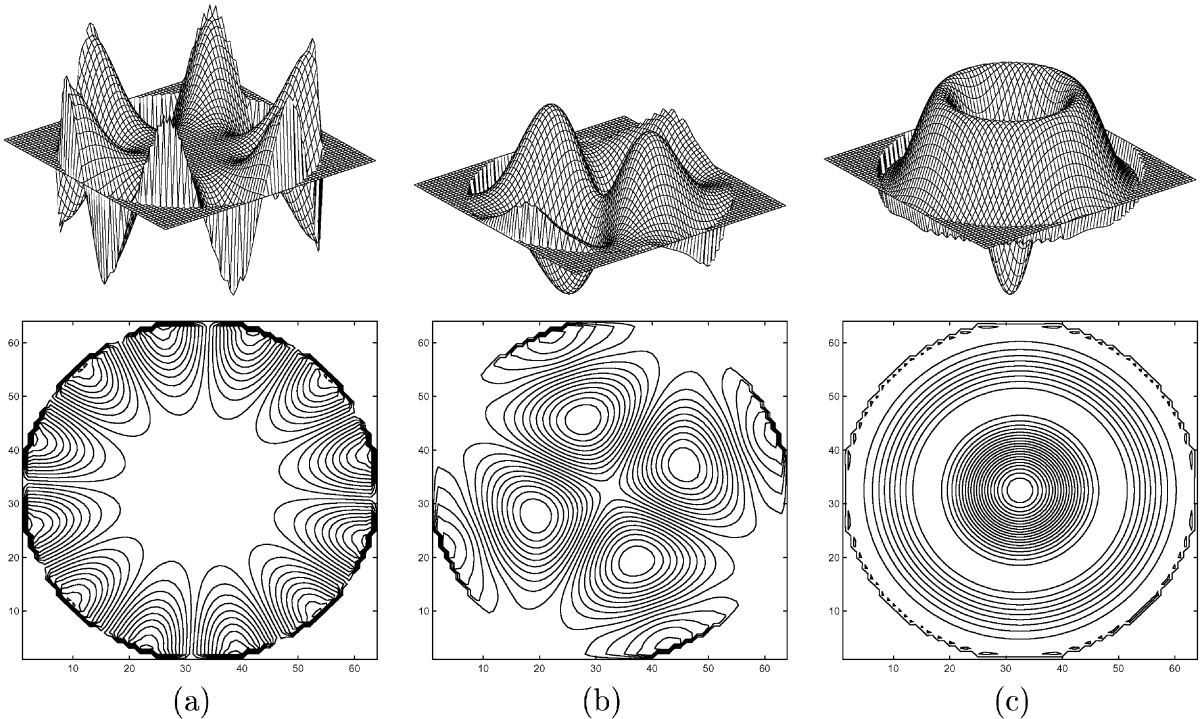


Fig. 10. Mesh and contour plots of ordered state patterns at $R = 7.0$: (a) $t = 730$; (b) $t = 480$; (c) $t = 780$. The corresponding principal Fourier–Bessel modes are $[1, 6]$, $[2, 2]$ and $[3, 0]$, respectively.

For a given m value, when R is large, it approximately takes a π increment in R to observe the pattern with one more ring of cells, i.e., the value of l increases 1.

Although the morphology of the ordered patterns appears diverse, it can be understood from the point of view of “energy”. The square of the ratio of $\mu_{l,m}$ and R is the “energy” of the linearized stationary Cahn–Hilliard equation ($E = \mu_{l,m}^2/R^2$). This value is 1 in the present case which is determined by the nontrivial eigenvalue of $\nabla^2(\nabla^2 + 1)\Psi = 0$. Therefore, all observed ordered state patterns approximately have the same energy. This degeneracy is due to the symmetry of the circular domain. The present findings of the mechanism of pattern selection might shed light on the control of microphase separation and pattern formation in more complicated systems in a circular domain.

In the present simulation, modal competition is often observed when the control parameter R is simultaneously close to two or more $\mu_{l,m}$ values. In this case, the formation of the ordered state patterns can be complicated by possible competition among different Fourier–Bessel modes since either mode $[l, m]$ or mode $[l', m']$ can be excited. Numerically, it is possible to observe two or more different patterns at a given control parameter.

A typical case of two-mode competition is observed at $R = 5.0$. Fig. 5 illustrates the phase diagram around $R = 5.0$. As shown in Fig. 5, the control parameter $R = 5.0$ is in the overlap region of two Fourier–Bessel modes $[2, 1]$ and $[1, 3]$, since the corresponding μ values of these two modes are $\mu_{2,1} = 5.331$ and $\mu_{1,3} = 4.403$, respectively. As a result, both these two Fourier–Bessel modes can be excited and compete to dominate the formation of ordered state patterns. Two typical ordered state patterns at different time steps are shown in Fig. 6, corresponding to the principal Fourier–Bessel modes $[2, 1]$ and $[1, 3]$, respectively. In Figs. 7 and 8, we depict the Fourier–Bessel decomposition

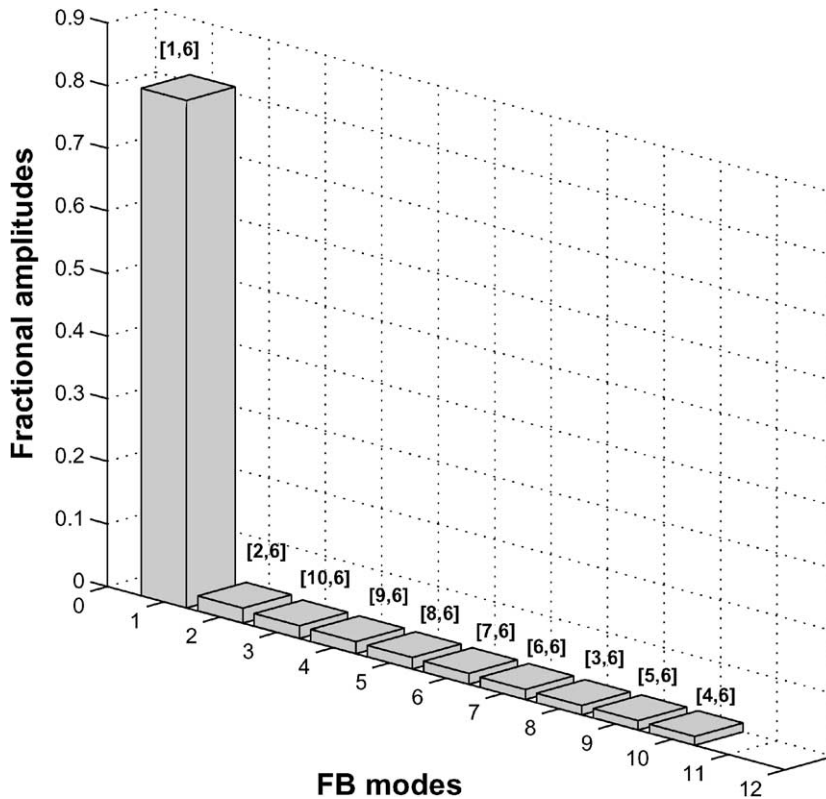


Fig. 11. Fourier–Bessel decomposition of the ordered state pattern shown in Fig. 10(a).

of these two ordered state patterns. It is clearly shown that for pattern Fig. 6(a), the principal Fourier–Bessel mode is [2, 1], while for pattern Fig. 6(b), the principal Fourier–Bessel mode is [1, 3].

With the increase of the control parameter, i.e., the size of the geometric domain, generally more Fourier–Bessel modes can be simultaneously excited. Thus the competition among these active modes can be expected to occur more frequently. For example, three principal Fourier–Bessel modes [1, 6] ($\mu_{1,6} = 7.501$), [2, 2] ($\mu_{2,2} = 6.706$) and [3, 0] ($\mu_{3,0} = 7.016$) have been observed to take part in the competition at $R = 7.0$. Once again, the control parameter value is close to these theoretical extrema of the Bessel function. Fig. 9 plots the phase diagram around $R = 7.0$. It is shown that the control parameter $R = 7.0$ is in the overlap region of the above-mentioned three Fourier–Bessel modes. Three typical ordered state patterns are shown in Fig. 10, corresponding to the principal Fourier–Bessel modes [1, 6], [2, 2] and [3, 0], respectively. This is further illustrated by the results of Fourier–Bessel decomposition of these three ordered state pattern, as shown in Figs. 11–13.

The intermediate “patterns” between two stable ordered state patterns are usually irregular as a result of the spontaneous multi-mode excitation. However, in some special cases, when the fractional amplitudes of two Fourier–Bessel modes are comparable to each other, these two modes will contribute together to dominate the pattern morphology. For example, Fig. 14(a) and (b) show two “mixed patterns” of such situation. Fourier–Bessel decomposition of these two “mixed patterns” are illustrated in Figs. 15 and 16. In the pattern shown in Fig. 14(a), the two dominant Fourier–Bessel modes are [3, 0] and [1, 6], with the fractional amplitudes $A_{3,0} = 0.379$ and $A_{1,6} = 0.293$, respectively. Similarly, for the pattern shown in Fig. 14(b), the two leading fractional amplitudes are $A_{3,0} = 0.337$ and $A_{1,6} = 0.298$, respectively. Since these two fractional amplitudes are of the same order, the corresponding

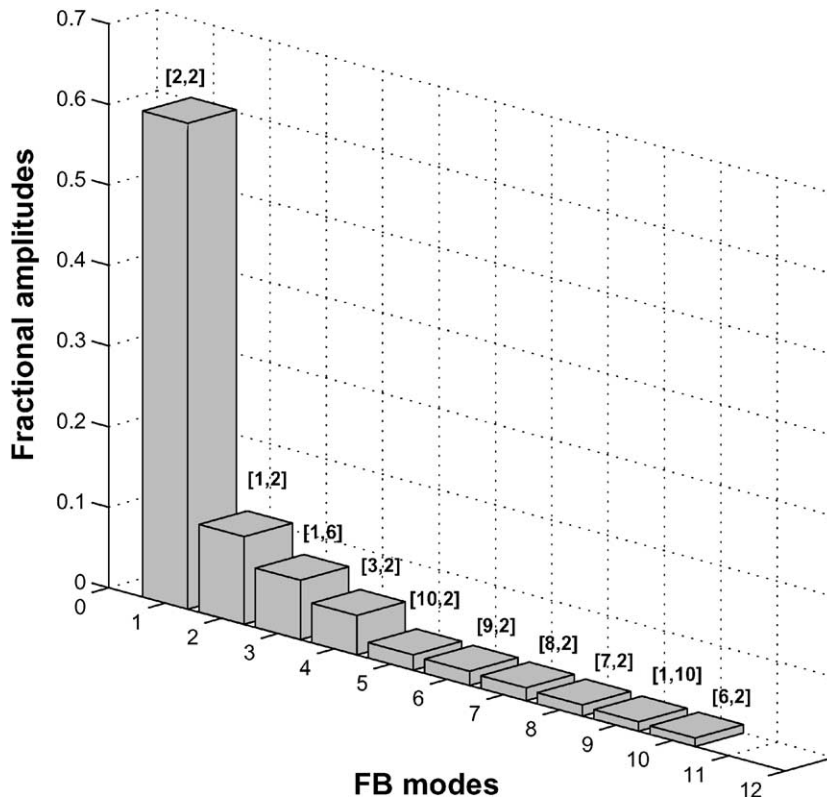


Fig. 12. Fourier–Bessel decomposition of the ordered state pattern shown in Fig. 10(b).

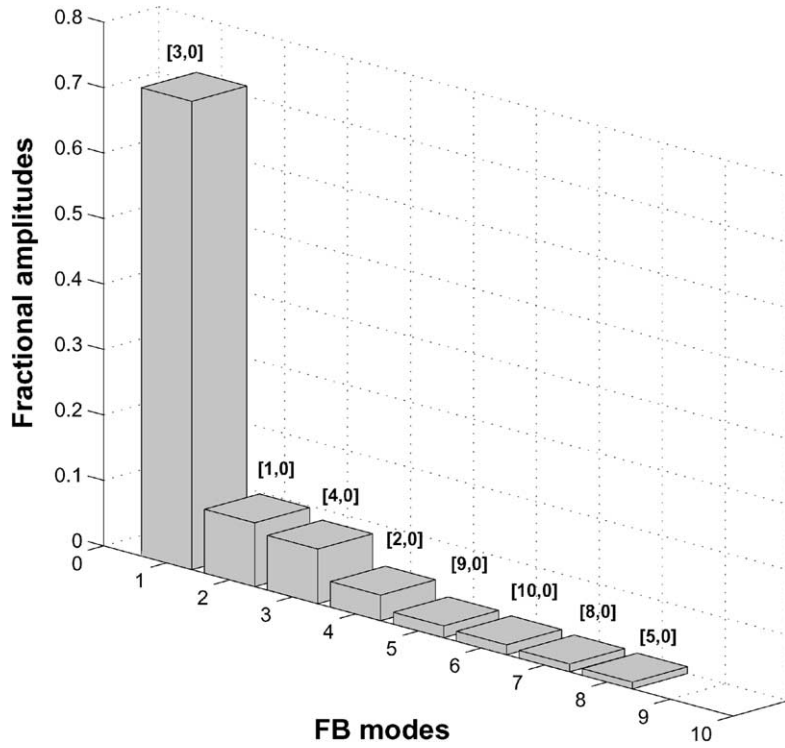


Fig. 13. Fourier–Bessel decomposition of the ordered state pattern shown in Fig. 10(c).

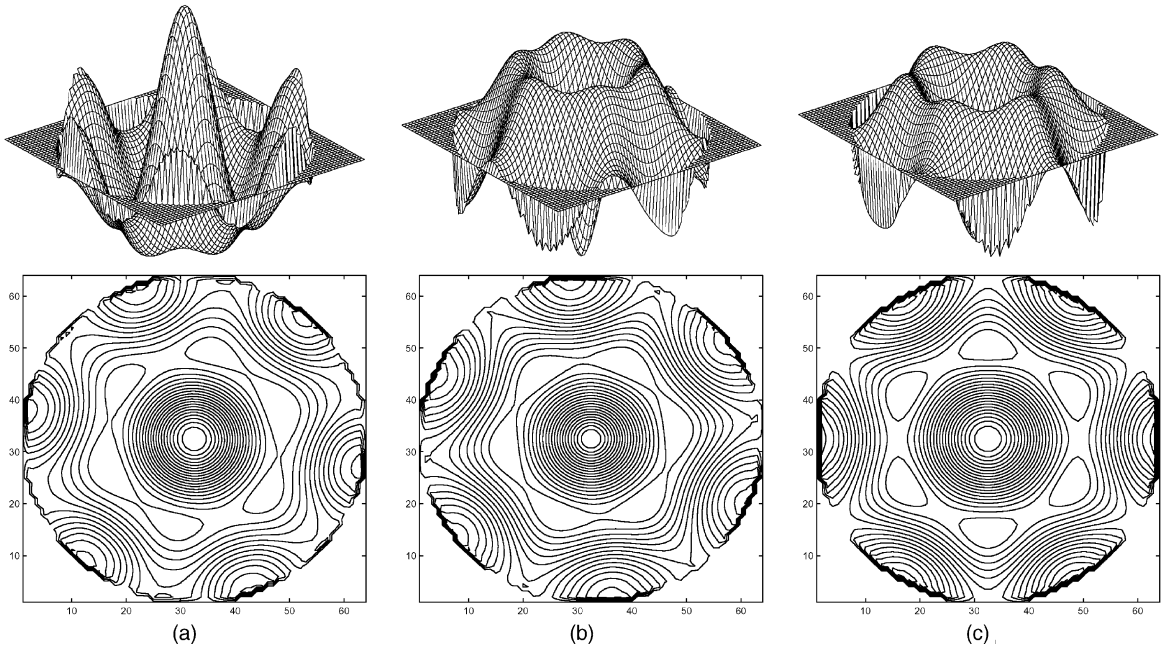


Fig. 14. Mesh and contour plots of the mixed patterns at $R = 7.0$: (a) $t = 520$; (b) $t = 970$; (c) a reconstructed pattern corresponds to the mixed pattern (b).

pattern morphology is mainly due to the contribution of these two competing Fourier–Bessel modes. This feature can be obviously seen in Fig. 14(a) and (b), especially in the contour plots. In Fig. 14(c), we depict a reconstructed pattern. It is obtained by the linear combination ($c_1\Phi_{3,0} + c_2\Phi_{1,6}$, where $c_1 = 0.337$ and $c_2 = 0.298$) of the two pure Fourier–Bessel modes [3, 0] and [1, 6]. Obviously, the reconstructed pattern, Fig. 14(c), resembles Fig. 14(b). Similar “mixed” cellular patterns have also been observed in the experiment of combustion flames [21]. It is found that the Fourier–Bessel decomposition provides a good explanation for the formation of such patterns.

Interestingly, the spatial distribution of the pattern shown in Fig. 14(a) is approximately a “mirror image” of the pattern shown in Fig. 14(b), i.e., the distribution of order parameter fields of these two patterns are symmetric. The occurrence of mirror images is due to the conservation of the order parameter, i.e., Eq. (8). Because of such a constraint, the phase separation can only occur as the order parameter polarization with respect to the (r, θ) plane. Thus, if Ψ is an ordered state of the system, $-\Psi$ should also be a possible ordered state of the system which has the symmetric distribution of the order parameter field as that of Ψ . In fact, these two patterns can be observed at the same control parameter R . Statistically, they should have equal probability to appear if the time integration is sufficiently long. Apart from these symmetric pairs of “mixed patterns”, the ordered state patterns shown in Figs. 3 and 10(c) are another example of approximate mirror patterns. They both are observed at control parameter $R = 7.0$.

Our computations are limited to the “small system” regime, i.e., the control parameter $R \leq 13$. So far, four complete classes ($l = 1-4$) of ordered state patterns have been observed. Both the confined circular geometry and the boundary condition are crucial factors in controlling the pattern morphology in the present case. Obviously, as the control parameter R continues to increase, other series of ordered state patterns ($l \geq 5$) can also be expected to

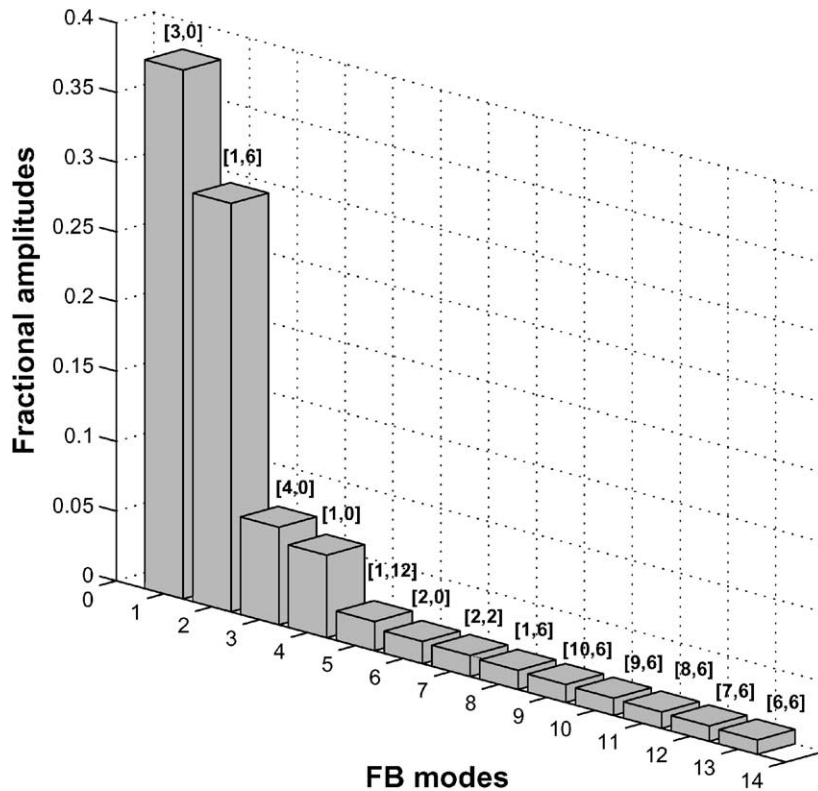


Fig. 15. Fourier–Bessel decomposition of the ordered state pattern shown in Fig. 14(a).

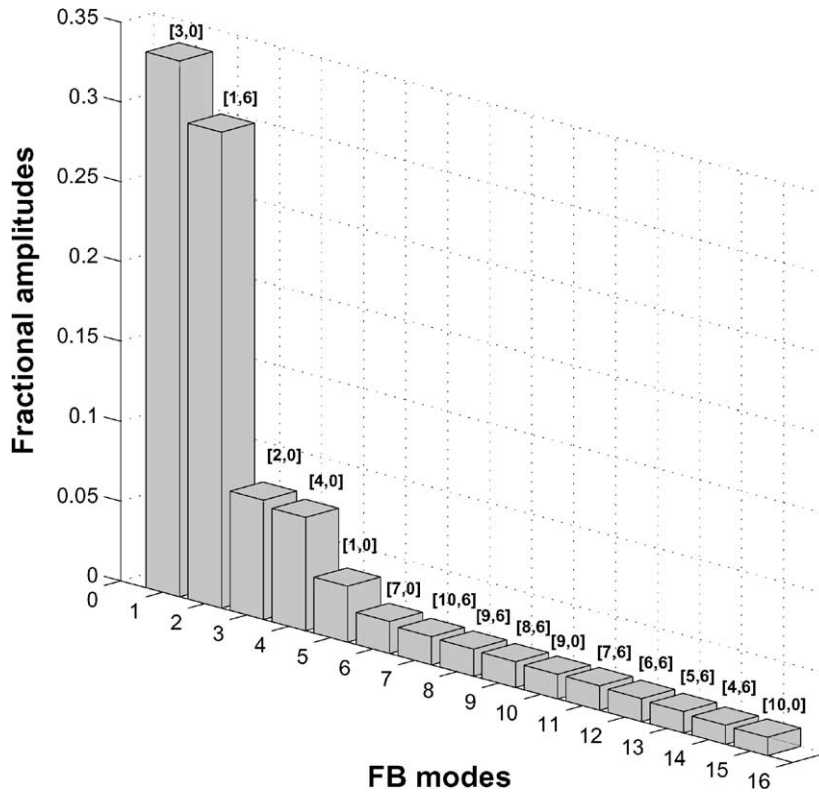


Fig. 16. Fourier–Bessel decomposition of the ordered state pattern shown in Fig. 14(b).

appear. When the system enters the “large system” regime, it is believed that there are more Fourier–Bessel modes that can be simultaneously excited at given control parameter. From the statistical point of view, the density of states (number of modes per unit radius) increases as the control parameter R increases on the circular domain for a given energy. As a consequence, the total pattern energy in this case distributes over a large number of modes rather than a few principal ones. This multi-mode excitation and competition usually destroy the spatially coherent structures and result in spatiotemporal chaos. In other words, the effect of geometry and boundary control will become less important for pattern formation and competition in such circumstance.

5. Conclusion

This paper investigates the effective control of the formation of the ordered state patterns in a confined circular domain. The Cahn–Hilliard equation with a zero-flux boundary condition is used as a theoretical model to simulate the phase separation and pattern formation in binary systems. High-precision numerical solutions are obtained by using a wavelet-based DSC algorithm. Theoretical analysis is carried out via the Fourier–Bessel decomposition. Four complete classes of cellular ordered state patterns have been obtained through extensive numerical simulations. For the present “small system” regime ($R \leq 13$), the size of the characteristic microphase domain is comparable with the size of the confined domain. Therefore, the pattern morphology is effectively controlled by the domain size, as well as the boundary condition. Usually a finite number of spatial modes can be excited when the domain size is

small. In such a case, the Fourier–Bessel analysis provides a good characterization of the ordered state patterns. In addition, the control mechanism of modal selection and modal competition has been revealed. The results of present numerical simulations and theoretical analysis not only provide understandings of self-assembly of supermolecules via phase separation conducted over spheres or cylinders, but also might shed light on the practical (experimental) design of supra- and supermolecules through phase separation in a confined circular domain.

Acknowledgements

This work was supported by the National University of Singapore.

References

- [1] P. Moriarty, Nanostructured materials, *Rep. Prog. Phys.* 64 (2001) 297.
- [2] M.A. Hillmyer, P.M. Lipic, D.A. Hajduk, K. Almdal, F.S. Bates, Self-assembly and polymerizations of epoxy resin–amphiphilic block copolymer nanocomposites, *J. Am. Chem. Soc.* 119 (1997) 2749.
- [3] J.S. Moore, Supramolecular polymers, *Curr. Opin. Colloid* 4 (1999) 108.
- [4] J.K. Cox, A. Eisenberg, R.B. Lennox, Patterned surfaces via self-assembly, *Curr. Opin. Colloid* 4 (1999) 52.
- [5] V. Percec, C.-H. Ahn, G. Ungar, D.J.P. Yeardley, M. Möller, S.S. Sheiko, Controlling polymer shape through the self-assembly of dendritic side-groups, *Nature* 391 (1998) 161.
- [6] N. Koneripalli, N. Singh, R. Levicky, F.S. Bates, P.D. Gallagher, S.K. Satija, Confined block copolymer thin films, *Macromolecules* 28 (1995) 2897.
- [7] G. Balzer, C. Denz, O. Knaup, T. Tschudi, Circling vortices and pattern dynamics in a unidirectional photorefractive ring oscillator, *Chaos, Soliton & Fractals* 10 (1999) 725.
- [8] H. Zhang, J. Zhang, Y. Yang, X. Zhou, Microphase separation of diblock copolymer induced by directional quenching, *J. Chem. Phys.* 106 (1997) 784.
- [9] A.V. Mamaev, M. Saffman, Selection of unstable patterns and control of optical turbulence by Fourier plane filtering, *Phys. Rev. Lett.* 80 (1998) 3499.
- [10] S.J. Jensen, M. Schwab, C. Denz, Manipulation, stabilization, and control of pattern formation using Fourier space filtering, *Phys. Rev. Lett.* 81 (1998) 1614.
- [11] S. Takeda, K. Koto, S. Iijima, T. Ichihashi, Nanoholes on silicon surface created by electron irradiation under ultrahigh vacuum environment, *Phys. Rev. Lett.* 79 (1997) 2994.
- [12] T. Kapitaniak, *Controlling Chaos: Theoretical and Practical Methods in Nonlinear Dynamics*, Academic Press, London, 1990–1996.
- [13] G. Hu, K.F. He, Controlling chaos in systems described by partial-differential equations, *Phys. Rev. Lett.* 71 (1993) 3794.
- [14] W. Lu, D. Yu, R.G. Harrison, Control of patterns in spatiotemporal chaos in optics, *Phys. Rev. Lett.* 76 (1996) 3316.
- [15] M.B. Tarlie, K.R. Elder, Metastable state selection in one-dimensional systems with a time-ramped control parameter, *Phys. Rev. Lett.* 81 (1998) 18.
- [16] S. Ciliberto, J.P. Gollub, Pattern competition leads to chaos, *Phys. Rev. Lett.* 52 (1984) 922.
- [17] A. Kudrolli, J.P. Gollub, Localized spatiotemporal chaos in surface waves, *Phys. Rev. E* 54 (1996) R1052.
- [18] S. Ciliberto, E. Pampaloni, C. Pérez-García, Competition between different symmetries in convective patterns, *Phys. Rev. Lett.* 61 (1988) 1198.
- [19] K. Lerman, D.S. Cannell, G. Ahlers, Analysis of transients for binary mixture convection in cylindrical geometry, *Phys. Rev. E* 59 (1999) 2975.
- [20] D.J. Tritton, *Physical Fluid Dynamics*, Oxford University Press, Oxford, 1988.
- [21] A. Palacios, G.H. Gunaratne, M. Gorman, K.A. Robbins, Cellular pattern formation in circular domains, *Chaos* 7 (3) (1997) 463.
- [22] H.M. Jaeger, S.R. Nagel, R.P. Behringer, Granular solids, liquids, and gases, *Rev. Mod. Phys.* 68 (1996) 1259.
- [23] P.B. Umbanhowar, F. Melo, H.L. Swinney, Periodic, aperiodic, and transient patterns in vibrated granular layers, *Physica A* 249 (1998) 1.
- [24] G.W. Wei, Discrete singular convolution for the solution of the Fokker–Planck equations, *J. Chem. Phys.* 110 (1999) 8930.
- [25] G.W. Wei, A unified approach for solving the Fokker–Planck equation, *J. Phys. A* 33 (2000) 4935.
- [26] G.W. Wei, Discrete singular convolution for the sine–Gordon equation, *Physica D* 137 (2000) 247.
- [27] Y.B. Zhao, G.W. Wei, Y. Xiang, Discrete singular convolution for the prediction of high frequency vibration of plates, *Int. J. Solids Struct.* 39 (2002) 65.
- [28] J.D. Gunton, M. San Miguel, P.S. Sahni, in: C. Domb, J.L. Lebowitz (Eds.), *Phase Transitions and Critical Phenomena*, vol. 8, Academic Press, London, 1983, pp. 267–482.

- [29] J.W. Cahn, J.E. Hilliard, Free energy of a nonuniform system. I. Interfacial free energy, *J. Chem. Phys.* 28 (1958) 258;
J.W. Cahn, J.E. Hilliard, Spinodal decomposition—a reprise, *Acta Metall.* 19 (1971) 151.
- [30] H. Furukawa, in: K. Kawasaki, M. Suzuki (Eds.), *Formation, Dynamics, and Statistics of Patterns*, vol. 2, World Scientific, Singapore, 1993, pp. 266–308.
- [31] A. Noveick-Cohen, L.A. Segel, Nonlinear aspects of the Cahn–Hilliard equation, *Physica D* 10 (1984) 277.
- [32] A.W. Leissa, *Vibration of Plates*, Published for the Acoustical Society of America through the American Institute of Physics, Washington, DC, 1993.
- [33] S. Rosenblat, S.H. Davis, G.M. Homsy, Nonlinear Marangoni convection in bounded layers. Part 1. Circular cylindrical containers, *J. Fluid Mech.* 120 (1982) 91.
- [34] G.N. Watson, *Theory of Bessel Functions*, Cambridge University Press, Cambridge, 1966.